Journal of Materials Chemistry A

ROYAL SOCIETY OF CHEMISTRY

PAPER

View Article Online
View Journal



Cite this: DOI: 10.1039/d5ta02253c

# Functional groups bridging the layers of nitrogen carbide nanosheets facilitate ultrafast interlayer charge transfer: *ab initio* nonadiabatic molecular dynamics simulations†

Huimin Gao,[ab] Wang Gong,[a] Anqi Shi,*[a] Xiuyun Zhang,[c] Xinxin Wang,[d] Yong Pu*[a] and Xianghong Niu*[a]

Two-dimensional (2D) layered nitrogen carbides (CN) are potential photocatalytic materials. However, their photocatalytic efficiency is severely constrained by the inefficient transfer and separation of the carriers, especially between layers. Herein, based on hybrid density functional theory and *ab initio* nonadiabatic molecular dynamics, we find the formation of interlayer type II band alignments in few-layer graphitic $C_3N_4$ (g-$C_3N_4$) through bridging functional groups (–$NH_2$, –COOH, and –OH), thus promoting the interlayer separation of photogenerated carriers. Specifically, functional groups facilitate the photogenerated carriers to overcome the Coulomb interaction in-plane and transfer between layers, benefiting from the disruption of symmetry and the formation of interlayer carrier transfer channels. Notably, the photoexcited carriers achieve ultrafast interlayer transfer on the fs timescale due to the strong nonadiabatic coupling of the interface transfer channel, suppressing the recombination of carriers with a timescale exceeding 10 ns. Furthermore, the hydrogen evolution reaction activity at the N site is enhanced due to the increased concentration of electrons, as indicated by the change in Gibbs free energy values ranging from −0.01 eV to 0.10 eV. Our work provides a feasible strategy to transfer interlayer carriers in layered 2D materials.

Received 19th March 2025
Accepted 11th July 2025

DOI: 10.1039/d5ta02253c

rsc.li/materials-a



## 1 Introduction

The rapid development of the economy has triggered a crisis in energy and environmental sustainability.[1–5] Providing clean and low-cost energy through solar-driven photocatalytic water splitting is a potential strategy.[6–11] In recent years, two-dimensional (2D) layered nitrogen carbides (CN) have become promising candidates for visible-light photocatalysis due to their fascinating merits, such as a large specific surface area, environmental friendliness, low cost, and a suitable band gap for photo-absorption.[12–15] However, the majority of photo-generated electrons and holes (PEHs) tend to recombine in-plane rather than migrate to the reaction site, due to the poor separation and transfer of interlayer carriers (see Fig. 1). There are two factors for the poor charge separation and transfer: (1) in single-phase 2D layered CN, the symmetry of the geometric and electronic structures between adjacent layers is unfavorable for interfacial charge transfer; (2) the absence of interlamellar connection channels results in an inherent barrier between the CN layer, which severely inhibits the effective interlayer carrier transfer.[16–18]

Establishing an interlayer "electric bridge" is a valid strategy to accelerate the transfer and separation of interlayer charge.[17–22] These "electric bridges", serving as the channel for charge transfer, are classified into three types: (1) inserting other 2D materials between CN layers, (2) reducing the distance experimentally, and (3) bridging signal atoms between layers. All three methods can facilitate interlayer charge separation and transfer. Nevertheless, they are all constrained by the inherent limitations of each strategy. For insertion, the transfer of free carriers between layers remains inefficient due to the existence of spatial site resistance, potential barriers, and coulombic interactions at the interface.[19] For reducing the distance experimentally, experimental preparation environments such as high temperatures have the potential to destroy the CN structure. For bridging signal atoms (such as Fe, Na, K, Cu, I, and Cu), the controllable insertion of single atoms remains

[a]School of Science, Institute of Advanced Materials (IAM), Nanjing University of Posts &Telecommunications, Nanjing 210023, China. E-mail: shianqi1222@163.com; puyong@njupt.edu.cn; xhniu@njupt.edu.cn

[b]College of Science, Jinling Institute of Technology, Nanjing 211169, China

[c]College of Physics Science and Technology, Yangzhou University, Yangzhou 225002, China

[d]School of Physics and Engineering, Henan Key Laboratory of Photoelectric Energy Storage Materials and Applications, Henan University of Science and Technology, Luoyang 471023, China

† Electronic supplementary information (ESI) available: Computation details. See DOI: https://doi.org/10.1039/d5ta02253c

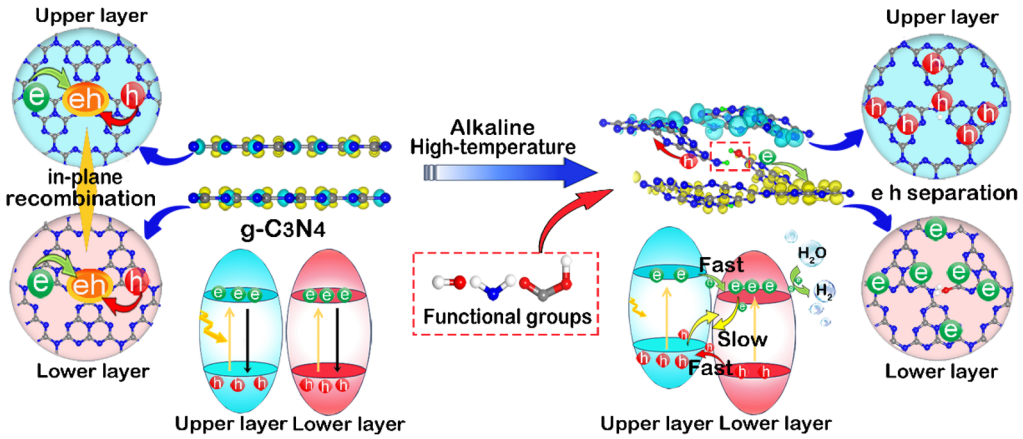


Fig. 1 Schematic illustration of the strategies for functional groups bridging the layered g-$C_3N_4$ between layers. The grey, blue, white, and red balls represent the C, N, H, and O atoms, respectively.

a huge challenge, and the metal atoms may contaminate the surrounding environment.[19,23–26] Therefore, the construction of an effective "electric bridge" by a convenient method remains a challenge. In fact, CN thin layers are prone to "cutting" during the experimental preparation, such as in alkaline or high temperature environments.[27] Meanwhile, a localized functional group "electric bridge" can be established at the cutting site, due to the firmly covalent bonds of C atoms and functional groups in the environment.[28–30] Functional groups act as the "electric bridge" to facilitate interlayer electron separation, and transfer would be a convenient and environmentally friendly approach. However, there is an absence of systematic exploration into the functional group-bridged layered CN materials.

In this work, taking the common functional groups (–$NH_2$, –COOH, and –OH) as an example, we systematically investigate the possibility of functional groups as the "electric bridge" between layers of graphene $C_3N_4$ (g-$C_3N_4$) by density functional theory and *ab initio* nonadiabatic molecular dynamics (NAMD). As expected, the functional groups can serve as an "electric bridge" for interlayer charge transfer (see Fig. 1). The introduction of functional groups breaks the interlayer symmetry of the g-$C_3N_4$ structure, resulting in an optimal charge distribution between the layers. The transfer timescale of electrons (holes) between the CBMs (VBMs) in the upper and lower layers is hundreds of femtoseconds, suggesting the spatial separation of electrons and holes. The recombination timescale of interlayer electrons and holes is in the tens of nanoseconds, indicating a lower recombination probability. Furthermore, the change in Gibbs free energy values for the hydrogen evolution reaction (HER) approaches 0 eV in the N site possessing high electron cloud density, indicating that the functional group-bridged g-$C_3N_4$ is an excellent catalyst for the photocatalytic HER from an activity perspective.

# 2 Results and discussion

## 2.1 Pristine g-$C_3N_4$

For pristine g-$C_3N_4$, as shown in Fig. S11,† the optimized lattice parameter is 7.14 Å, consistent with the previously reported result of 7.135 Å.[31] According to previous studies, the ABAB-type is the most stable stacking method, in which the g-$C_3N_4$ units of the upper layer are almost fully situated on the open hollow site of the adjacent lower layer.[32] Therefore, ABAB-type stacking is employed in this study. The interlayer distance is about 3.3 Å, indicating a typical van der Waals interaction between the layers and the significant difficulty of interlayer transfer of electrons and holes (see Fig. S11†).

The band structure of few-layer g-$C_3N_4$ exhibits a direct bandgap, with equal energy band contributions from both the upper layer and the adjacent lower layer (see Fig. 2a), suggesting the degeneracy of the upper layer and the lower layer energy bands.

For two-dimensional condensed phase systems, the influence of excited states on configuration may be weaker than that of the thermal fluctuations of atoms; therefore, the classical path approximation (CPA) was used in NAMD.[33,34] Based on the CPA theory, the distribution of the photoexcited carrier is represented by the distribution of ground-state carriers in theoretical simulations. In this context, we calculate the photogenerated carriers' distribution at the conduction band minimum (CBM) and valence band maximum (VBM) in few-layer g-$C_3N_4$. As shown in Fig. 2c and S13,† the photogenerated electrons are distributed on the C atoms and some N atoms in both upper and lower layers, while the photogenerated holes are distributed on the N atoms in both upper and lower layers. Clearly, the N atom will be the recombination center of PEHs. Additionally, the average distribution of PEHs in the upper and lower layers leads to the recombination of PEHs in the same layer. The characteristics of the energy bands and charge distributions severely inhibit the photocatalytic efficiency of g-$C_3N_4$.

## 2.2 Functional group-bridged g-$C_3N_4$

**2.2.1 Screen structure.** In general, the carbon–nitrogen (C–N) bonds in g-$C_3N_4$ thin layers are susceptible to "cutting" during the experimental preparation, such as in alkaline or high temperature environments. Concurrently, the formation of a localized interlayer "electronic bridge" is probable, as C atoms

 

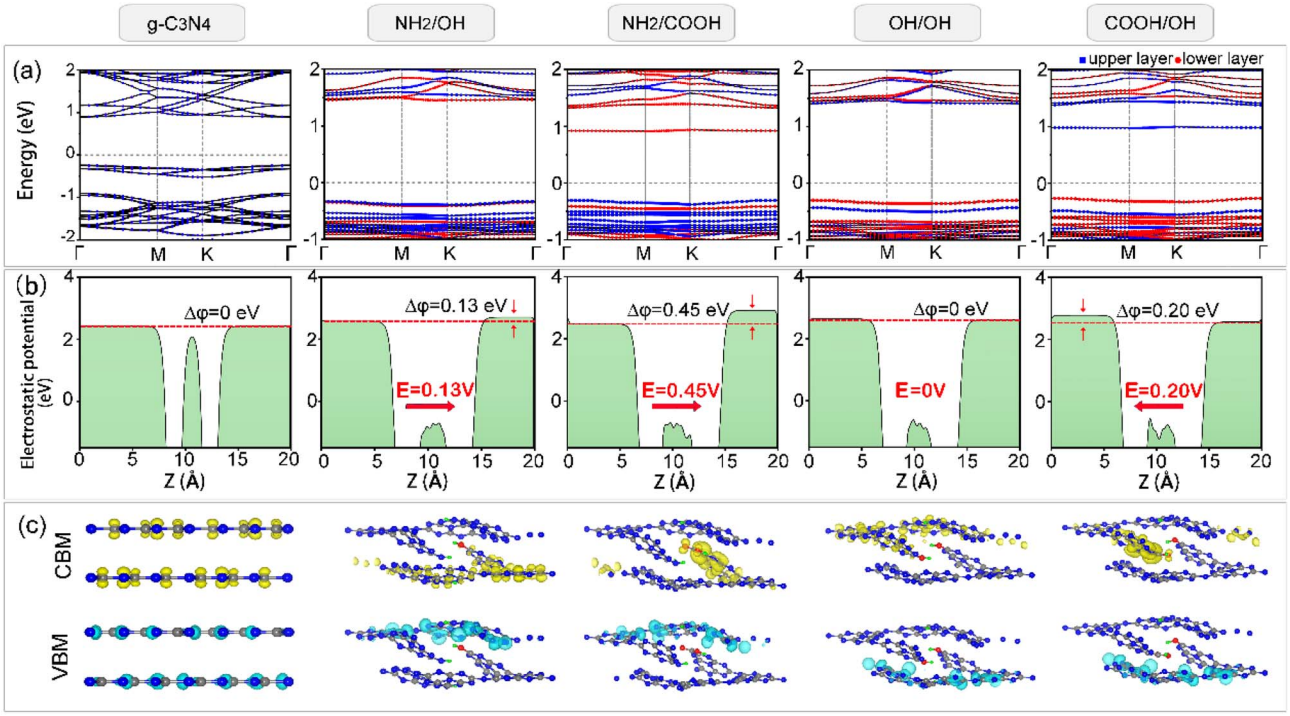


Fig. 2 (a) The band structure of pristine g-$C_3N_4$ and $NH_2$/OH, $NH_2$/COOH, OH/OH, and COOH/OH bridged g-$C_3N_4$. The blue and red represent the contribution of the upper and the lower layers. (b) Electrostatic potential along the *z*-direction of g-$C_3N_4$ and $NH_2$/OH, $NH_2$/COOH, OH/OH, and COOH/OH bridged g-$C_3N_4$. The red arrow represents the direction of the electric field. (c) The photogenerated carriers' distribution at the CBM and VBM for g-$C_3N_4$ and $NH_2$/OH, $NH_2$/COOH, OH/OH, and COOH/OH bridged g-$C_3N_4$. Yellow represents electron convergence, and blue represents electron dissipation. The value of the isosurface is 0.0015 e bohr$^{-3}$.

exhibit a strong affinity for functional groups in the environment through covalent bonding. In this study, we consider the case of bridging –$NH_2$, –OH, and –COOH with the C atoms. The possible bridging structures include: $NH_2$/$NH_2$ (where the C atom in the upper layer bridges to the $NH_2$ group, and the C atom in the lower layer also bridges to the $NH_2$ group), $NH_2$/OH, $NH_2$/COOH, OH/OH, COOH/OH/, and COOH/COOH bridged g-$C_3N_4$ (see Fig. S11†). The $NH_2$/$NH_2$ bridged g-$C_3N_4$ is excluded due to large structural distortion after optimization (see Fig. S11†). For COOH/COOH bridged structures, the CBM and VBM are equally contributed by the upper and lower levels in bridged structures (see Fig. S12†). This energy structure leads to a recombination of PEHs similar to pristine g-$C_3N_4$; thus, the COOH/COOH is also deemed unsuitable as an electronic bridge. For $NH_2$/OH, $NH_2$/COOH, OH/OH or OH/COOH bridged structures, the CBM and VBM are contributed by different layers respectively, leading to interlayer type II band alignments (see Fig. 2a). The type II band alignments can facilitate the charge transfer between the upper and lower layers, promoting the spatial separation of PEHs (see Fig. S14†). Therefore, considering both the structural stability and energy band alignment, we select $NH_2$/OH, $NH_2$/COOH, OH/OH, and OH/COOH bridged g-$C_3N_4$ to explore the influence of functional groups as "electric bridges" on interlayer separation and transfer of PEHs.

**2.2.2 Carrier dynamics of functional group-bridged g-$C_3N_4$.** First, to assess the effect of the type II band alignment on the carriers' separation, we calculate the photogenerated carriers' distribution at the CBM and VBM (see Fig. 2c). Compared with the average charge distribution on the VBM and CBM in pristine g-$C_3N_4$, the photogenerated electrons (holes) are concentrated in the lower (upper) layer in $NH_2$/ON and $NH_2$/COOH bridged g-$C_3N_4$. For OH/OH and COOH/OH bridged structures, the electrons (holes) are distributed in the upper (lower) layer. That is, photogenerated carriers overcome the Coulomb interaction in-plane, achieving an optimal distribution in the upper and lower layers. This behavior is attributed to both the symmetry destruction of the g-$C_3N_4$ geometry through environment "cutting" and the functional group bridging.

Then, the built-in electric field also plays a crucial role in the separation of photogenerated carriers due to its electric field force on carriers.[35] The electrostatic potential along the *z*-direction of g-$C_3N_4$ and functional group-bridged g-$C_3N_4$ is shown in Fig. 2b. The built-in electric fields pointing to the upper layer with magnitudes of 0.13 V or 0.45 V are observed in $NH_2$/OH and $NH_2$/COOH bridged g-$C_3N_4$, facilitating the transfer of electrons (holes) from the upper layer's CBM (the lower layer's VBM) to the lower layer's CBM (the upper layer's VBM). This further promotes the formation of the type II energy band alignment in $NH_2$/OH and $NH_2$/COOH bridged g-$C_3N_4$. In COOH/OH bridged g-$C_3N_4$, the built-in electric field is directed towards the lower layer with a value of 0.2 V, which promotes the aggregation of electrons (holes) in the CBM of the upper layer (VBM of the lower layer) to form a type II energy band alignment. For OH/OH bridged g-$C_3N_4$, although there is no

built-in electric field, it still possesses the type II energy band alignment. Combining the results of the energy band alignment, charge distribution, and built-in electric field, the PEHs are spatially separated in $NH_2$/OH, $NH_2$/COOH, OH/OH, and COOH/OH bridged g-$C_3N_4$. This is essential to enhance the g-$C_3N_4$ photocatalytic efficiency.

Next, to further understand the impact of bridging functional groups on the carriers' transfer, we employ the NAMD method with the photogenerated electrons (holes) on the CBM (VBM) energy states of the functional group-bridged g-$C_3N_4$ with a type II band alignment.[36,37] Fig. 3a–e exhibits the transfer and separation processes of PEHs. Specifically, for pristine g-$C_3N_4$, photogenerated electrons are excited from the VBM to the CBM, where the VBM and the CBM are co-contributed by the upper and lower layers, implying that the photogenerated electron holes are prone to complexation (see Fig. 3a). For $NH_2$/OH and $NH_2$/COOH bridged g-$C_3N_4$, photogenerated electrons transfer from the CBM of the upper layer to the adjacent conduction band of the lower layer, and photogenerated holes transfer from the VBM of the lower layer to the adjacent valence band of the upper layer (see Fig. 3b and c). In contrast, for OH/OH and COOH/OH bridged g-$C_3N_4$, photogenerated electrons (holes) transfer from the CBM of the lower layer (VBM of the upper layer) to the adjacent conduction band of the upper layer (the valence band of the lower layer) (see Fig. 3d and e). The ultrafast interlayer transfer process is observed for PEHs in $NH_2$/OH, $NH_2$/COOH, OH/OH, and COOH/OH bridged g-$C_3N_4$. For photogenerated electrons, their transfer timescale in the CBM of the interlayer ranges from 192 fs to 630 fs (see Fig. 3g–j), while the transfer timescales for holes in the VBM of the interlayer are around 200 fs. The rapid transfer of PEHs between donor and acceptor states indicates that functional group bridging facilitates the swift spatial separation of PEHs.

The occupation time of PEHs in their acceptor states after separation is also critical for the photocatalytic reaction. A prolonged occupation of PEHs in the acceptor state without recombination can provide sufficient oxidants and reductants for redox reactions. Therefore, it is necessary to calculate the recombination lifetime of the separated PEHs between layers. The timescales for interlayer recombination in pristine g-$C_3N_4$ and $NH_2$/OH, $NH_2$/COOH, OH/OH, and COOH/OH bridged g-$C_3N_4$ are shown in Fig. 3f, adopting $P(t) = \exp(-t/\tau)$ exponential function.[38] The timescale of pristine g-$C_3N_4$ is approximately 3.00 ns, consistent with the previous finding.[32] After the introduction of functional groups, the time scales of interlayer recombination are found to be significantly extended, ranging from 10.81 ns to 26.15 ns. The NAMD calculations demonstrate that PEHs not only achieve ultrafast interlayer separation but also maintain prolonged occupation in the acceptor state within functional group-bridged g-$C_3N_4$, thereby ensuring the PEHs' participation in catalytic reactions.

The differences in the above charge transfer between layers are related to the nonadiabatic coupling strength between donor and acceptor states. A stronger coupling parameter correlates with faster charge transfer rates.[39,40] Fig. 4a–d exhibits the averaged absolute values of the nonadiabatic coupling between different electronic states around the Fermi level. Clearly, the nonadiabatic coupling between neighboring states

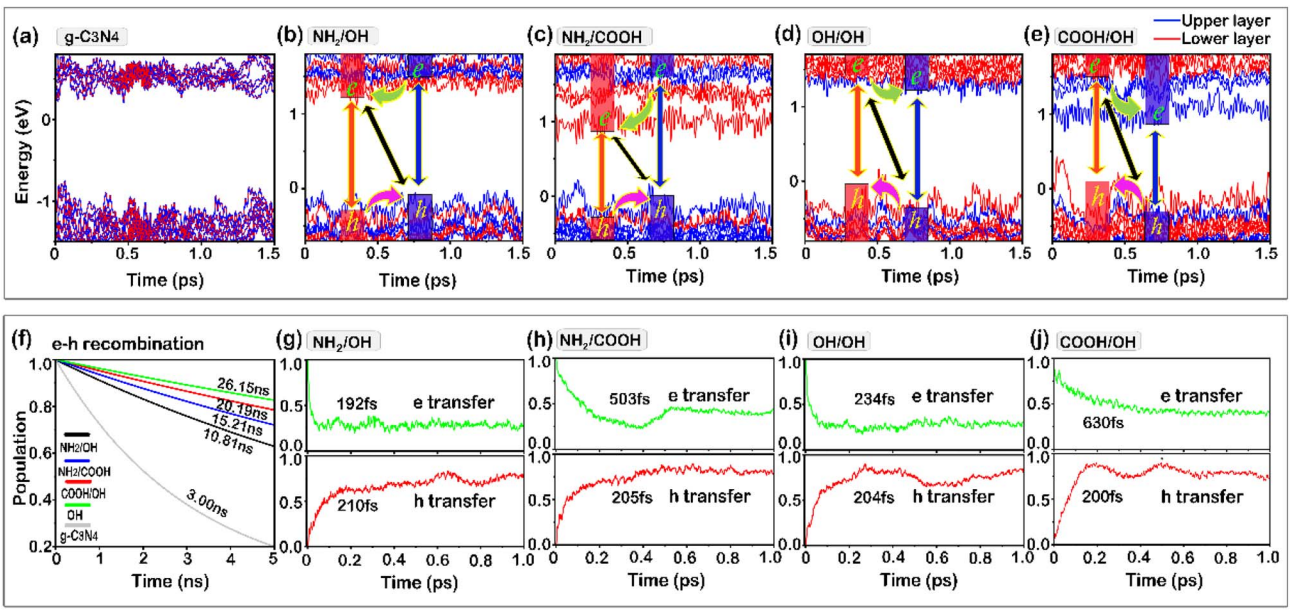


Fig. 3 (a)–(e) The evolution of the energy states around the Fermi level for pristine g-$C_3N_4$ and $NH_2$/OH, $NH_2$/COOH, OH/OH, and COOH/OH bridged g-$C_3N_4$. The zero represents the Fermi level. The blue and red energy states represent the contribution of the upper and lower layers, respectively. The inset represents the recombination and transfer channel of photogenerated carriers. The black (blue and red) arrow represents the interlayer (intralayer) recombination of photogenerated carriers, and the green (purple) arrow represents the electron (hole) transfer in the interlayer. (f) The interlayer recombination of photogenerated carriers of pristine g-$C_3N_4$ and $NH_2$/OH, $NH_2$/COOH, OH/OH, and COOH/OH bridged g-$C_3N_4$. (g)–(j) The intralayer transfer of photogenerated carriers of $NH_2$/OH, $NH_2$/COOH, OH/OH, and COOH/OH bridged g-$C_3N_4$. Blue (red) represents the transfer of electrons (holes).

 

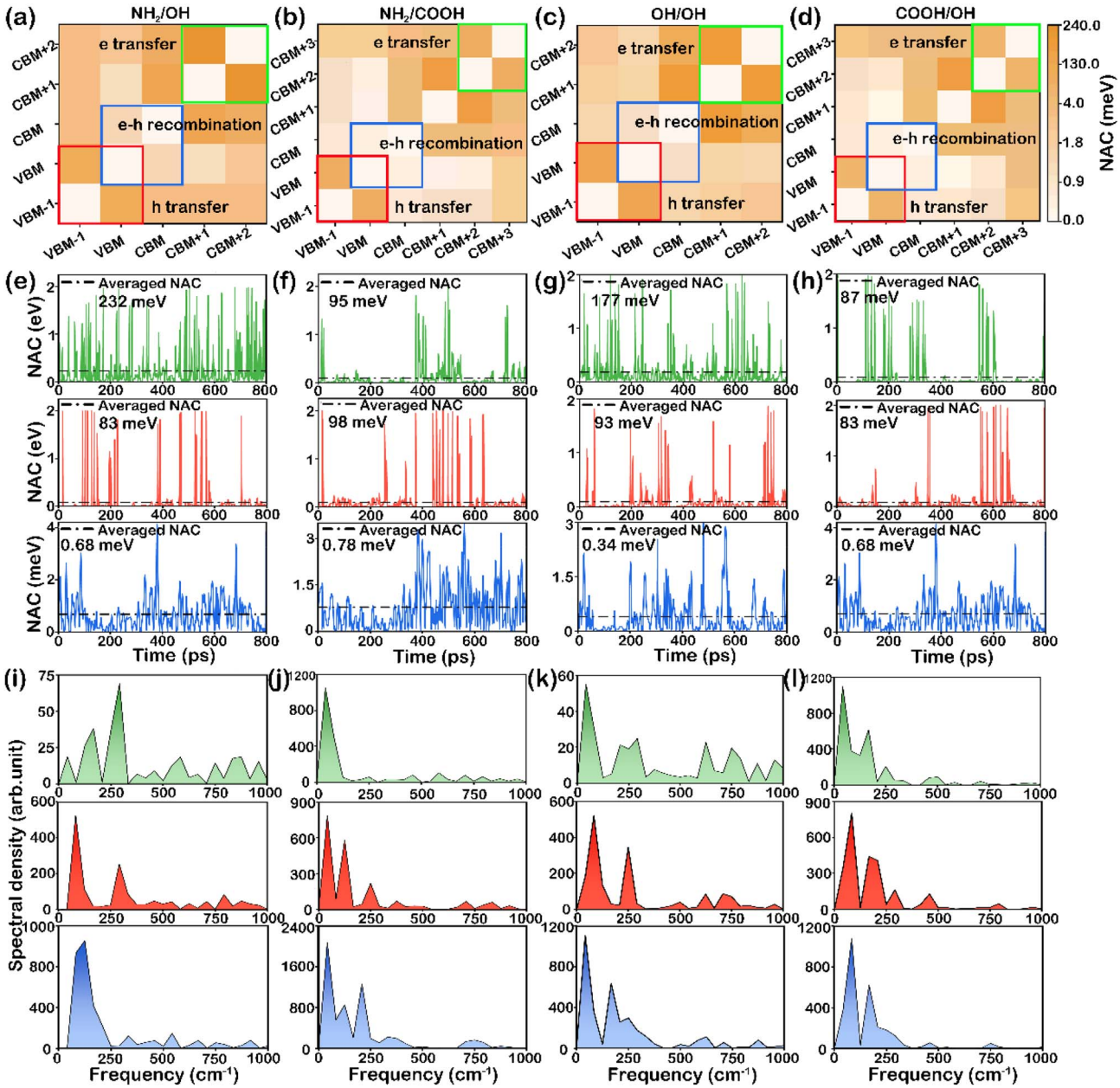


Fig. 4 (a)–(d) Averaged absolute values of the nonadiabatic coupling between different electronic states around the Fermi level for $NH_2$/OH, $NH_2$/COOH, OH/OH, and COOH/OH bridged g-$C_3N_4$. (e)–(h) The time-dependent evolution of the nonadiabatic coupling between electronic states dominating the photogenerated electron transfer (green line), hole transfer (red line), and recombination of PEHs (blue line) between layers. (i)–(l) Fourier transforms of autocorrelation functions for the energy difference functions between electronic states involving photogenerated electron transfer (green line), hole transfer (red line), and recombination of PEHs (blue line) between layers.

is stronger than that of the separated states, which demonstrates that the interlayer transfer pathway of PEHs is indeed composed of the neighboring states.

The nonadiabatic coupling elements of photogenerated electron (hole) transfer and carriers' recombination are indicated by green (red) and blue lines (see Fig. 4a–d), respectively. Taking the example of the $NH_2$/OH bridged functional group, the electron–hole complexation is calculated between the CBM and VBM (as shown in the blue line of Fig. 4a). The transfer of electrons between the layers is calculated between the CBM + 2 and the CBM + 1 (as shown in the green line of Fig. 4a), and the transfer of holes between the layers is calculated between the VBM and VBM − 1 (as shown in the red line of Fig. 4a). The corresponding time-dependent evolutionary processes of nonadiabatic coupling elements are displayed in Fig. 4e–h. Obviously, for the interlayer electron transfer of functional group-bridged g-$C_3N_4$, the average values of the nonadiabatic coupling elements are 232, 177, 95, and 87 meV ($NH_2$/OH > OH/OH > $NH_2$/COOH > COOH/OH), respectively. This result is in accordance with the trend of the interlayer electron transfer

lifetimes with 192, 234, 503, and 630 fs ($NH_2$/OH < OH/OH < $NH_2$/COOH < COOH/OH) (see Fig. 3g–j). For the interlayer hole transfer of functional group-bridged g-$C_3N_4$, the average values of the nonadiabatic coupling elements are approximately 90 meV. The timescales of their corresponding hole transfers are around 200 fs (see Fig. 3g–j). For the recombination of interlayer PEHs, the average values of the nonadiabatic coupling elements are found to be relatively small (less than 1 meV). This indicates the weak nonadiabatic correlation between the two energy states and low recombination of PEHs, corresponding with the longer recombination time (exceeding 10.81 ns) in Fig. 3f. Therefore, the timescale of the interlayer charge transfer is positively correlated with the value of nonadiabatic coupling elements between the donor and acceptor states.

In fact, the nonadiabatic coupling elements are influenced by two primary factors: (1) the energy difference between donor and acceptor states, and (2) the electron–phonon coupling term. As shown in Fig. 3b–e, the energy differences for interlayer electron transfer of $NH_2$/OH and OH/OH bridged g-$C_3N_4$ are notably smaller than those of $NH_2$/COOH and COOH/OH bridged g-$C_3N_4$. This phenomenon suggests that electrons can be transferred faster between $NH_2$/OH and OH/OH bridged g-$C_3N_4$ layers. The energy differences for interlayer hole transfer are comparable, indicating similar transfer energy barriers and times for holes. The energy differences for interlayer PEH recombination of $NH_2$/COOH and COOH/OH bridged g-$C_3N_4$ are smaller than those of $NH_2$/OH and OH/OH bridged g-$C_3N_4$, demonstrating the relatively high probability of recombination for $NH_2$/COOH and COOH/OH bridged g-$C_3N_4$.

For the electron–phonon coupling term, the corresponding phonon mode can be visualized by employing the Fourier transforms (FT) of the autocorrelation functions (see Fig. 4i–l).[41] The main phonon modes are concentrated in low-frequency modes below 300 $cm^{-1}$, which mainly come from the strong interlayer interaction.[42,43] The presence of low-frequency phonons indicates the existence of the electron–phonon coupling, which generally allows carrier transfer. $NH_2$/OH and OH/OH bridged g-$C_3N_4$ exhibits repaid interlayer electron transfer, but the strength of the phonons is generally weaker than that of $NH_2$/COOH and COOH/OH bridged g-$C_3N_4$. This suggests that phonon coupling differences have less effect on nonadiabatic coupling elements than energy differences between donor and acceptor states. For the interlayer hole transfer or interlayer recombination of PEHs in functional group-bridged g-$C_3N_4$, the strength of the phonon is comparable, suggesting a comparable contribution of phonon for nonadiabatic coupling elements. Additionally, compared with OH and $NH_2$, COOH is easy to capture photogenerated electrons due to the strong polarity and π bonds.[44] As illustrated in Fig. 2c, the photogenerated electrons are localised around COOH in $NH_2$/COOH and COOH/OH bridged g-$C_3N_4$, whereas the electrons are distributed on CN layers in the $NH_2$/OH and OH/OH bridged g-$C_3N_4$. The attraction of COOH for photogenerated electrons suppresses electron transfer (see Fig. 3h and j).

**2.2.3 Photoabsorption and surface activity of functional group-bridged g-$C_3N_4$.** Finally, we evaluate the photoabsorption and surface activity of functional group-bridged g-$C_3N_4$, which are also essential for an efficient photocatalyst. The photoabsorption spectra of g-$C_3N_4$ and functional group-bridged g-$C_3N_4$ are shown in Fig. 5a, based on the HSE06. The first absorption peak of pristine g-$C_3N_4$ occurs at an energy of 3.37 eV, consistent with the previous results (3.35 eV).[45] Compared with pristine g-$C_3N_4$, the first absorption peaks of functional group-bridged g-$C_3N_4$ exhibit a redshift, indicating good optical correspondence of functional group-bridged g-$C_3N_4$. The improvement of energy conversion efficiency is a significant target in the pursuit of solar energy utilization for photocatalytic water splitting. We calculate the solar-to-hydrogen conversion efficiency ($\eta_{STH}$) using standard AM1.5G spectra (see Table S1†). The $\eta_{STH}$ achieves 17.2% and 19.2% in $NH_2$/COOH and COOH/OH bridged g-$C_3N_4$, significantly higher than the 10.3% of pristine g-$C_3N_4$. $NH_2$/OH and OH/OH bridged g-$C_3N_4$ exhibits suboptimal solar energy conversion efficiency, with the $\eta_{STH}$ of 6.7% and 7.2%, respectively.

The HER activity can be assessed under standard conditions by employing the Gibbs free energy change of hydrogen adsorption ($\Delta G_H$). The conventional HER pathway involves the initial state $H^+$, the intermediate state *H, and the 1/2$H_2$ states. The $\Delta G_H$ of the intermediate state *H reflects the HER activity. As an ideal photocatalyst for the HER, the value of $\Delta G_H$ should approach zero ($\Delta G_H \approx 0$). Generally, the N site is considered to

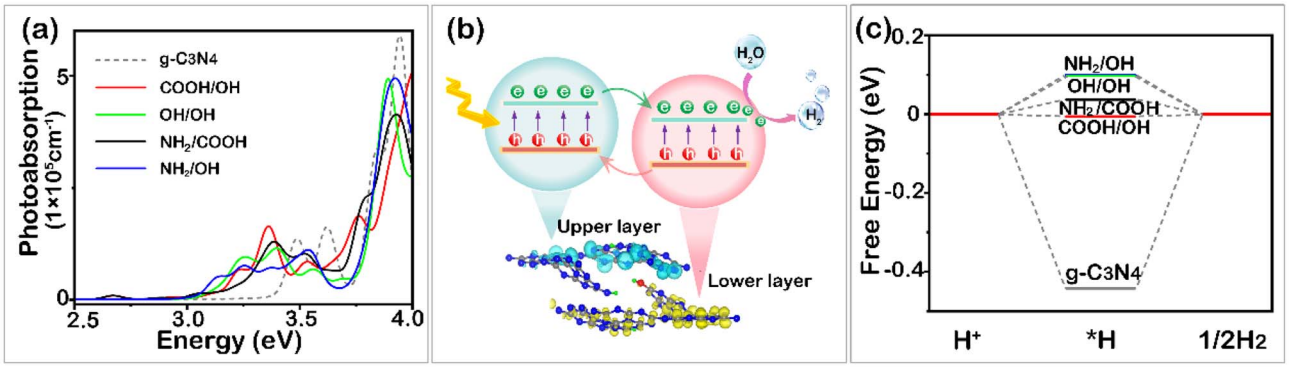


Fig. 5 (a) The photoabsorption spectra of g-$C_3N_4$ and functional group-bridged g-$C_3N_4$. (b) Schematic diagram of the photocatalytic reaction. (c) $\Delta G_H$ for the HER of g-$C_3N_4$ and functional group-bridged g-$C_3N_4$.

 

be the HER site of CN. The $\Delta G_H$ value on the N site of pristine g-$C_3N_4$ is −0.45 eV (Fig. 5c). After bridging functional groups, the $\Delta G_H$ values notably decrease, ranging from −0.01 eV to 0.10 eV. This phenomenon can be attributed to the reduction in the adsorption of H at the N site where electrons are aggregated, benefiting from the interlayer separation of PEHs. The broad photoabsorption and good surface activity make the functional group-bridged g-$C_3N_4$ more suitable for application in the photocatalytic HER.

# 3 Conclusions

In summary, we explored the influence of functional groups bridging the layers of g-$C_3N_4$ on the interlayer transfer and separation of carriers. The functional groups can serve as a bridge between the layered g-$C_3N_4$, facilitating the transfer and separation of interlayer PEHs. After bridging functional groups, the ultrafast transfer of electrons (holes) between layers is achieved on the fs timescale, and the recombination lifetime of the interlayer PEHs exceeds 10 ns. This prevents the recombination of PEHs in the interlayer and in the plane, and provides an abundance of oxidants and reductants for the photocatalytic reaction. Moreover, as the photocatalysts for the HER, the photoabsorption and hydrogen evolution ability of functional group-bridged g-$C_3N_4$ is enhanced compared with that of pristine g-$C_3N_4$. This study provides not only effective photocatalysts for the HER but also a feasible strategy to achieve efficient interlayer charge separation in 2D layered photocatalysts.

# Data availability

The authors confirm that the data required to reproduce the findings of this study are available within the article and its ESI.† The results can be reproduced using density functional theory calculations.

# Author contributions

Huimin Gao: investigation, conceptualisation, writing – original draft, methodology, data curation. Wang Gong: writing – review & editing, formal analysis, project administration. Aiqi Shi: writing – review & editing, resources, data curation. Xiuyun Zhang: writing – review & editing, software. Xinxin Wang: writing – review & editing, data curation. Yong Pu: writing – review & editing, supervision, project administration. Xianghong Niu: writing – review & editing, supervision, project administration, funding acquisition.

# Conflicts of interest

The authors declare no competing financial interest.

# Acknowledgements

This work was supported by the National Natural Science Foundation of China (Grant No. 22473060 and 12304297), the Six Talent Peaks project in Jiangsu Province (Grant No. XCL-104) and China Scholarship Council program (Project ID: 202308320237).

# References

1 I. Ahmed, M. Rehan, A. Basit, S. H. Malik, W. Ahmed and K.-S. Hong, *Renewable Energy*, 2024, **223**, 119944.
2 N. Mohammed, H. Lian, M. S. Islam, M. Strong, Z. Shi, R. M. Berry, H.-Y. Yu and K. C. Tam, *Chem. Eng. J.*, 2021, **417**, 129237.
3 M. Sadiq, R. Shinwari, M. Usman, I. Ozturk and A. I. Maghyereh, *Nucl. Eng. Technol.*, 2022, **54**, 3299–3309.
4 J. Gong, S. Ji, J. Li, H. Wei, W. Mao, J. Hu, W. Huang, X. He, X. a. Li and L. Chu, *Sci. China Mater.*, 2024, **67**, 2848–2855.
5 Z. Xiao, X. Xiao, L. B. Kong, H. Dong, X. Li, B. He, S. Ruan, J. Zhai, K. Zhou, Q. Huang and L. Chu, *Int. J. Extreme Manuf.*, 2024, **6**, 022006.
6 I. Ahmad, G. Li, A. Al-Qattan, A. J. Obaidullah, A. Mahal, M. Duan, K. Ali, Y. Y. Ghadi and I. Ali, *Mater. Today Sustainability*, 2024, **25**, 100666.
7 Y. Ma, Y. Liu, Y. Bian, A. Zhu, Y. Yang and J. Pan, *J. Colloid Interface Sci.*, 2018, **518**, 140–148.
8 R. Yang, Y. Fan, Y. Zhang, L. Mei, R. Zhu, J. Qin, J. Hu, Z. Chen, Y. Hau Ng, D. Voiry, S. Li, Q. Lu, Q. Wang, J. C. Yu and Z. Zeng, *Angew. Chem., Int. Ed.*, 2023, **62**, e202218016.
9 A. Shi, D. Sun, R. Guan, W. Shan, Z. Qin, J. Wang, L. Wei, S. Zhou, X. Zhang and X. Niu, *J. Phys. Chem. Lett.*, 2023, **14**, 1918–1927.
10 H. Gao, A. Shi, R. Guan, Z. Xin, X. Zhang, B. Wang, Y. Pu and X. Niu, *Appl. Phys. Lett.*, 2024, **124**, 253901.
11 L. Chu, H. Shen, H. Wei, H. Chen, G. Ma and W. Yan, *Int. J. Miner., Metall. Mater.*, 2024, **32**, 498–503.
12 W. J. Ong, L. L. Tan, Y. H. Ng, S. T. Yong and S. P. Chai, *Chem. Rev.*, 2016, **116**, 7159–7329.
13 Y. Zhang, T. Mori, J. Ye and M. Antonietti, *J. Am. Chem. Soc.*, 2010, **132**, 6294–6295.
14 R. Guan, A. Shi, X. Zhang, B. Wang, Y. Li and X. Niu, *ACS Catal.*, 2024, **14**, 18580–18589.
15 L. Chu, Z. Rong, M. Ma, F. Guo, S. Tian and J. Yang, *Prog. Nat. Sci.: Mater. Int.*, 2025, **35**, 215–221.
16 J. Zhang, X. Tan, L. Shi, H. Chen, Y. Liu, S. Wang, X. Duan, M. Wu, H. Sun and S. Wang, *Appl. Catal., B*, 2023, **333**, 122781.
17 J. Shen, C. Luo, S. Qiao, Y. Chen, Y. Tang, J. Xu, K. Fu, D. Yuan, H. Tang, H. Zhang and C. Liu, *ACS Catal.*, 2023, **13**, 6280–6288.
18 X. Xiao, Y. Gao, L. Zhang, J. Zhang, Q. Zhang, Q. Li, H. Bao, J. Zhou, S. Miao, N. Chen, J. Wang, B. Jiang, C. Tian and H. Fu, *Adv. Mater.*, 2020, **32**, 2003082.
19 P. M. Ismail, S. Ali, S. Ali, J. Li, M. Liu, D. Yan, F. Raziq, F. Wahid, G. Li, S. Yuan, X. Wu, J. Yi, J. S. Chen, Q. Wang, L. Zhong, Y. Yang, P. Xia and L. Qiao, *Adv. Mater.*, 2023, **35**, 2303047.
20 K. Liu, J. Li, H. Qi, M. Hambsch, J. Rawle, A. R. Vázquez, A. S. Nia, A. Pashkin, H. Schneider, M. Polozij, T. Heine,

M. Helm, S. C. B. Mannsfeld, U. Kaiser, R. Dong and X. Feng, *Angew. Chem., Int. Ed.*, 2021, **60**, 13859–13864.
21 J. Duan, G. Qin, L. Min, Y. Yang and C. Wang, *ACS Appl. Mater. Interfaces*, 2018, **10**, 38084–38092.
22 A. Shi, R. Guan, J. Lv, B. Wang, Z. Niu, W. Zhang and X. Niu, *npj Comput. Mater.*, 2024, **24**, 01384.
23 L. Qin, J. Meng, G. Yang, Y. Pan, X. Gao, Y. Yang and Y. Guo, *Appl. Catal., B*, 2024, **345**, 123695.
24 L. Liu, F. Chen, J. Wu, J. Chen and H. Yu, *Proc. Natl. Acad. Sci. U. S. A.*, 2022, **120**, e2215305120.
25 T. Xiong, W. Cen, Y. Zhang and F. Dong, *ACS Catal.*, 2016, **6**, 2462–2472.
26 H. Gao, S. Yan, J. Wang, Y. A. Huang, P. Wang, Z. Li and Z. Zou, *Phys. Chem. Chem. Phys.*, 2013, **15**, 18077–18084.
27 G. Zhang, J. Zhu, Y. Xu, C. Yang, C. He, P. Zhang, Y. Li, X. Ren and H. Mi, *ACS Catal.*, 2022, **12**, 4648–4658.
28 M. Rezaei, A. Nezamzadeh-Ejhieh and A. R. Massah, *Ecotoxicol. Environ. Saf.*, 2024, **269**, 115927.
29 X. Li, H. Mai, X. Wang, Z. Xie, J. Lu, X. Wen, S. P. Russo, D. Chen and R. A. Caruso, *J. Mater. Chem. A*, 2024, **12**, 5204–5214.
30 L. Kong, X. Cao, K. Liang, R. Wang, J. Liu, W. Shi and C. Lu, *J. Phys. Chem. C*, 2023, **127**, 13493–13502.
31 L. Guo, R. Li, J. Jiang, J.-J. Zou and W. Mi, *J. Mater. Chem. A*, 2021, **9**, 26266–26276.
32 X. Niu, Y. Yi, X. Bai, J. Zhang, Z. Zhou, L. Chu, J. Yang and X. Li, *Nanoscale*, 2019, **11**, 4101–4107.
33 A. V. Akimov and O. V. Prezhdo, *J. Chem. Theory Comput.*, 2013, **9**, 4959–4972.
34 Z. Zhang, W.-H. Fang, M. V. Tokina, R. Long and O. V. Prezhdo, *Nano Lett.*, 2018, **18**, 2459–2466.
35 X. Niu, X. Bai, Z. Zhou and J. Wang, *ACS Catal.*, 2020, **10**, 1976–1983.
36 L. Song, Z. Lin, Z. Zhang, Y. Fan and M. Zhao, *J. Catal.*, 2025, **447**, 116118.
37 P. Das, A. Ghosh and P. Sarkar, *ACS Appl. Mater. Interfaces*, 2024, **16**, 62043–62051.
38 X. Yu, Y. Su, W.-w. Xu and J. Zhao, *J. Phys. Chem. Lett.*, 2021, **12**, 2312–2319.
39 L. Zhang, W. Chu, Q. Zheng, A. V. Benderskii, O. V. Prezhdo and J. Zhao, *J. Phys. Chem. Lett.*, 2019, **10**, 6151–6158.
40 K. G. Reeves, A. Schleife, A. A. Correa and Y. Kanai, *Nano Lett.*, 2015, **15**, 6429–6433.
41 S. Sannigrahi, A. Ghosh, B. Ball and P. Sarkar, *J. Phys. Chem. C*, 2022, **126**, 20852–20863.
42 Y. Zhu, O. V. Prezhdo, R. Long and W.-H. Fang, *J. Am. Chem. Soc.*, 2023, **145**, 22826–22835.
43 R. Zhang, L. Zhang, Q. Zheng, P. Gao, J. Zhao and J. Yan, *J. Phys. Chem. Lett.*, 2018, **9**, 5419–5424.
44 Z. Teng, N. Yang, H. Lv, S. Wang, M. Hu, C. Wang, D. Wang and G. Wang, *Chem*, 2019, **5**, 664–680.
45 B. R. Bhagat and A. Dashora, *Carbon*, 2021, **178**, 666–677.

 